Parametric non-intrusive reduced-order models via operator inference for large-scale rotating detonation engine simulations

Ionuț-Gabriel Farcaș *
The University of Texas at Austin, Austin, TX, 78712

Rayomand P. Gundevia †
Jacobs Engineering Group, Inc., Edwards AFB, CA 93524

Ramakanth Munipalli‡
Air Force Research Laboratory, Edwards AFB, CA 93524

Karen E. Willcox§
The University of Texas at Austin, Austin, TX, 78712

This paper investigates the construction of unsteady parametric non-intrusive reduced-order models (ROMs) for large-scale, realistic rotating detonation rocket engine (RDRE) combustion chambers, with the end goal of employing these reduced models to accelerate the design optimization of RDREs. The large computational cost of the corresponding high-fidelity simulations restricts the number of parametric instances that can realistically be simulated to generate training data. Moreover, the resulting training data sets are often sparse and comprise down-sampled time instants from the high-fidelity simulation. This paper's goal is therefore to assess the potential of constructing accurate and predictive data-driven parametric ROMs for these challenging unsteady problems. To this end, we employ the operator inference (OpInf) procedure, which learns structure-preserving ROMs for systems with polynomial structure, without needing access to the high-fidelity simulator source code. To mitigate the challenge associated with training parametric ROMs using data from only a low number of parameter instances, we approximate the parametric dependence of the ROM operators via a Taylor expansion. We consider RDRE simulations for two injector designs, for which the corresponding high-fidelity simulations require more than $10,000$ cores and 5–10 million CPU-hours to simulate 1–2 ms of physical time. We consider parametric variations in the mass flow-rate and equivalence ratio. Our results are promising and show that OpInf can be used to construct accurate parametric ROMs from sparse training sets for parametric predictions outside of the training set and for predictions beyond the temporal training horizon.

I. Introduction

Recent advances in computational science and high-performance computing enable the simulation of complex real-world problems, such as three-dimensional reactive flows, with ever-increasing realism and accuracy; however, these simulations remain computationally expensive even on large supercomputers. This prevents straightforward approaches to many-query applications, such as uncertainty quantification and (design) optimization, which require ensembles of such computationally expensive simulations. Therefore, reduced-order models (ROMs) — aimed at replacing the computationally expensive high-fidelity model without deteriorating the overall accuracy — are instrumental for accelerating or even enabling these tasks in realistic problems.

This work focuses on the construction of parametric non-intrusive ROMs for realistic rotating detonation rocket engine (RDRE) combustion chambers using data obtained from a large-scale large-eddy simulation (LES) model. While LES solvers have matured in recent times in providing high quality data to address performance, stability and realizability concerns in the RDRE, ROMs can play an increasingly important role. The long-term goal of our research

*Postdoctoral fellow, Oden Institute for Computational Engineering and Sciences, ionut.farcas@austin.utexas.edu, AIAA Member.
†Aerospace Research Engineer, rayomand.gundevia.ctr@afrl.af.mil, AIAA Member.
‡Senior Aerospace Research Engineer, Combustion Devices, ramakanth.munipalli@us.af.mil, AIAA Senior Member.
§Director, Oden Institute for Computational Engineering and Sciences, kwillcox@oden.utexas.edu, AIAA Fellow.

Distribution Statement A: Approved for Public Release; Distribution is Unlimited. PA# AFRL-2022-5626

is to construct accurate and predictive parametric ROMs to accelerate the design optimization of RDREs. Constructing parametric ROMs for RDRE combustion chambers is motivated by the fact that, on the one hand, design optimization of individual RDRE components (injector, nozzle, etc.) in isolation is undesirable due to the strong coupling between them and, on the other hand, parametric analyses of the entire system are computationally infeasible at the present time. The rotating detonation engine concept involves fuel injection in an axially symmetric chamber (such as an annulus) wherein, once ignited at suitable conditions, a system of spinning detonation waves is produced (see Bykovskii et al. [1] for a detailed description). There are propulsive advantages to such an engine cycle in addition to its mechanical simplicity, and this has made the RDRE an active area of research in recent years.

Parametric ROMs for RDRE combustion chambers can be beneficial for a number of reasons. Notable among these are (i) an improved understanding of design feasibility, (ii) characterizing engine limit cycle behavior, and (iii) geometric optimization of these devices. Parametric ROMs [2] have been extensively used in aerospace engineering in previous research efforts. For example, Bui-Thanh et al. [3] used linearized parametric intrusive ROMs for probabilistic analysis of unsteady aerodynamic applications. In [4], parametric ROMs of unsteady aerodynamics were used for hypersonic vehicles. Furthermore, [5] proposed an adaptive sampling procedure for parametric reduced modeling of aeroelastic systems based on Krylov-subspace projections and interpolation. A two-step online method for interpolating projection-based linear parametric ROMs was proposed in [6]. Machine learning models were considered in [7] for constructing parametric ROMs of inviscid transonic flows past an airfoil. To efficiently reduce large data sets, [8] employed randomized algorithms for non-intrusive parametric reduced modeling. A Koopman operator-based approach was used in [9] for parametric non-intrusive reduced models for design optimization and uncertainty quantification via Monte Carlo sampling. In the frequency domain, [10] used parametric ROMs for the unsteady vortex-lattice method. Nevertheless, the task of constructing accurate and predictive ROMs for RDRE combustion chambers is far from easy. One challenge is the complexity of the physical phenomena that characterize the strongly unsteady and shock-dominated reacting flow. This complexity goes beyond the physical problems considered in the parametric ROM examples cited above. Another challenge is that the large computational cost of the high-fidelity simulation restricts the number of parameter instances that can realistically be simulated to generate training data. Even more, the corresponding data sets are often sparse — albeit large scale — and contain down-sampled time instants from the simulation code (because it is infeasible to store snapshots at every timestep in a simulation of this nature).

To tackle these challenges, we employ the operator inference (OpInf) framework [11]. OpInf is a scientific machine learning approach that learns from high-dimensional simulation data polynomial ROMs for systems whose governing equations contain polynomial nonlinearities. For more general types of nonlinearities, lifting transformations can be employed to expose (sometimes approximate) polynomial structure in the lifted governing equations [12]. To address the challenge of constructing parametric ROMs from only a few parametric instances, we approximate the parametric dependence of the reduced operators of the OpInf ROM via a Taylor expansion around a nominal parameter value; a similar approach was used in [3] to accelerate many-query applications via linearized parametric intrusive ROMs. We note that OpInf was employed in reactive flows in previous research efforts to construct data-driven non-intrusive ROMs for predictions beyond the training horizon for the truncated CVRC injector element in both 2D [13, 14] and 3D [15]. Our previous work in [16] used an enhanced version of OpInf for predictions beyond the training temporal horizon for the combustion chamber of the 45° sector of the RDRE scenario previously studied in [17]. In that work, the OpInf ROM was shown to be accurate and predictive when trained using sparse data sets containing down-sampled time instants from the high-fidelity simulation.

In this work, we go one step further and use OpInf for *parametric* reduced modeling of RDRE combustion chambers. We consider two RDRE injector designs characterized by two different oxidizer-to-fuel area ratios and impingement-cavity recess distances. The considered parametric variations are mass flow-rate and equivalence ratio. These variations are characterized in our model using a scalar parameter that depends on a weighted combination of normalized mass flow-rate and equivalence ratio. We emphasize the extreme scarcity of simulation training data: for the first injector design, we have simulation data for three parameter instances, while for the second injector design, we have data for two parameter instances.

The remainder of this paper is organized as follows. Section II introduces the problem setup and summarizes the OpInf approach used to construct data-driven parametric unsteady ROMs. Section III summarizes the setup for the parametric RDRE simulations considered in this work. Section IV presents the construction of parametric OpInf ROMs from data for large-scale, realistic three-dimensional RDRE combustion chambers with 34 million degrees of freedom. Section V concludes the paper.

Distribution Statement A: Approved for Public Release; Distribution is Unlimited. PA# AFRL-2022-5626

II. Parametric non-intrusive reduced-order modeling via discrete operator inference

A. Problem setup

Consider a parameter $\boldsymbol{\mu} \in \mathcal{D}$ in the domain $\mathcal{D} \subset \mathbb{R}^d$ of dimension $d \in \mathbb{N}$ and consider the time interval $[t_\mathrm{i}, t_\mathrm{f}]$, with t_i the initial time and t_f the final time. Define the state vector $\mathbf{q}(t;\boldsymbol{\mu}) = [q_1(t;\boldsymbol{\mu}), q_2(t;\boldsymbol{\mu}), \ldots, q_n(t;\boldsymbol{\mu})]^\top \in \mathbb{R}^n$ with $n \in \mathbb{N}$, where n is typically large. After spatial discretization, the dynamics of the given problem are modeled as a system of nonlinear ordinary differential equations (ODEs)

$$\frac{\mathrm{d}\mathbf{q}}{\mathrm{d}t}(t;\boldsymbol{\mu}) = \mathbf{f}(\mathbf{q}, t;\boldsymbol{\mu}), \quad \mathbf{q}(t_\mathrm{i};\boldsymbol{\mu}) = \mathbf{q}_\mathrm{init}(\boldsymbol{\mu}), \tag{1}$$

where $\mathbf{q}_\mathrm{init}(\boldsymbol{\mu})$ is a specified initial condition and $\mathbf{f} : \mathbb{R}^n \times [t_\mathrm{i}, t_\mathrm{f}] \times \mathcal{D} \to \mathbb{R}^n$ is a nonlinear function that defines the time evolution of the system state. The above system of ODEs represent the underlying system of discretized partial differential equations (PDEs) and the dimension n scales with the (large) dimension of the spatial discretization.

Let $\boldsymbol{\mu}_1, \boldsymbol{\mu}_2, \ldots, \boldsymbol{\mu}_m$ be $m \in \mathbb{N}$ parameter instances and let $\mathbf{q}_k(\boldsymbol{\mu}_j)$ denote the state solution at time t_k for parameter instance $\boldsymbol{\mu}_j$ where we use the notation $\mathbf{q}_k(\boldsymbol{\mu}_j) \equiv \mathbf{q}(t_k;\boldsymbol{\mu}_j)$. We collect mn_t snapshots over $[t_i, t_f]$, where n_t denotes the number of time instants for each parameter instance $\boldsymbol{\mu}_j$, by solving the high-fidelity model (1) for each $\boldsymbol{\mu}_1, \boldsymbol{\mu}_2, \ldots, \boldsymbol{\mu}_m$ and recording the solutions at the n_t time instants. Given an instance $\boldsymbol{\mu}_j$, we define the trajectory $\mathbf{Q}(\boldsymbol{\mu}_j) = \left[\mathbf{q}_1(\boldsymbol{\mu}_j), \mathbf{q}_2(\boldsymbol{\mu}_j), \ldots, \mathbf{q}_{n_t}(\boldsymbol{\mu}_j)\right]^\top$. The snapshot matrix $\mathbf{Q}$ collects the trajectories for all m parameter instances:

$$\mathbf{Q} = \begin{bmatrix} \mathbf{Q}(\boldsymbol{\mu}_1) & \mathbf{Q}(\boldsymbol{\mu}_2) & \cdots & \mathbf{Q}(\boldsymbol{\mu}_m) \end{bmatrix} \in \mathbb{R}^{n \times mn_t}.$$

Typically we have $mn_t \ll n$. Given this snapshot matrix, we learn parametric data-driven ROMs using the discrete OpInf approach.

B. Learning data-driven parametric reduced models via non-intrusive discrete operator inference

OpInf learns parametric reduced models with polynomial structure, where the structure is specified by the underlying governing equations [11]. In the first step, we compute the thin singular value decomposition of the snapshot matrix $\mathbf{Q}$:

$$\mathbf{Q} = \mathbf{U}\boldsymbol{\Sigma}\mathbf{V}^\top,$$

to determine the representation of the snapshots in a low-dimensional subspace, where $\mathbf{U} \in \mathbb{R}^{n \times mn_t}$, $\boldsymbol{\Sigma} \in \mathbb{R}^{mn_t \times mn_t}$, and $\mathbf{V} \in \mathbb{R}^{mn_t \times mn_t}$. $\boldsymbol{\Sigma}$ is a diagonal matrix containing the singular values of $\mathbf{Q}$ in non-decreasing order $\sigma_1 \geq \sigma_2 \geq \ldots \geq \sigma_{mn_t}$, where σ_j denotes the jth singular value. The reduced proper orthogonal decomposition (POD) basis $\mathbf{U}_r \in \mathbb{R}^{n \times r}$ comprises the first $r \ll n$ columns of $\mathbf{U}$, that is, the left singular vectors corresponding to the r largest singular values. Note that the POD basis $\mathbf{U}_r$ is independent of the parameter $\boldsymbol{\mu} \in \mathcal{D}$. We next compute the low-dimensional representation of the snapshots in the reduced-order linear subspace spanned by $\mathbf{U}_r$

$$\hat{\mathbf{Q}} = \mathbf{U}_r^\top \mathbf{Q} \in \mathbb{R}^{r \times mn_t}.$$

We first summarize the time-continuous or semi-discrete OpInf. To determine the parametric reduced operators that define the semi-discrete ROM, OpInf solves a linear least-squares problem. For example, for a ROM with quadratic form

$$\frac{\mathrm{d}\hat{\mathbf{q}}}{\mathrm{d}t}(t;\boldsymbol{\mu}) = \hat{\mathbf{A}}_\mathrm{sd}(\boldsymbol{\mu})\hat{\mathbf{q}}(t;\boldsymbol{\mu}) + \hat{\mathbf{H}}_\mathrm{sd}(\boldsymbol{\mu})\left(\hat{\mathbf{q}}(t;\boldsymbol{\mu}) \otimes \hat{\mathbf{q}}(t;\boldsymbol{\mu})\right), \quad \hat{\mathbf{q}}_\mathrm{init}(\boldsymbol{\mu}) = \mathbf{U}_r^\top \mathbf{q}_\mathrm{init}(\boldsymbol{\mu}), \tag{2}$$

we must determine the reduced operators $\hat{\mathbf{A}}_\mathrm{sd}(\boldsymbol{\mu}) \in \mathbb{R}^{r \times r}$ and $\hat{\mathbf{H}}_\mathrm{sd}(\boldsymbol{\mu}) \in \mathbb{R}^{r \times r^2}$, where the subscript sd denotes *semi-discrete* operators. In this parametric setting, we must represent in some way the parametric dependence of the operators $\hat{\mathbf{A}}_\mathrm{sd}$ and $\hat{\mathbf{H}}_\mathrm{sd}$. We employ a Taylor series expansion to achieve this (see, for example, [3]). Let $\boldsymbol{\mu}_0 \in \mathbb{R}^d$ denote the nominal parameter value around which the Taylor series expansions are performed. Denote the components of $\boldsymbol{\mu} = [\mu_1, \mu_2, \ldots, \mu_d] \in \mathbb{R}^d$ and let $\boldsymbol{\nu} = \boldsymbol{\mu} - \boldsymbol{\mu}_0 \in \mathbb{R}^d$. We have:

$$\hat{\mathbf{A}}_\mathrm{sd}(\boldsymbol{\mu}) = \hat{\mathbf{A}}_\mathrm{sd}|_{\boldsymbol{\mu}=\boldsymbol{\mu}_0} + \left.\frac{\mathrm{d}\hat{\mathbf{A}}_\mathrm{sd}}{\mathrm{d}\mu_1}\right|_{\boldsymbol{\mu}=\boldsymbol{\mu}_0} \nu_1 + \left.\frac{\mathrm{d}\hat{\mathbf{A}}_\mathrm{sd}}{\mathrm{d}\mu_2}\right|_{\boldsymbol{\mu}=\boldsymbol{\mu}_0} \nu_2 + \cdots + \left.\frac{\mathrm{d}\hat{\mathbf{A}}_\mathrm{sd}}{\mathrm{d}\mu_d}\right|_{\boldsymbol{\mu}=\boldsymbol{\mu}_0} \nu_d + \text{H.O.T.} \tag{3}$$

Distribution Statement A: Approved for Public Release; Distribution is Unlimited. PA# AFRL-2022-5626

and

$$\hat{\mathbf{H}}_{\mathrm{sd}}(\boldsymbol{\mu}) = \hat{\mathbf{H}}_{\mathrm{sd}}|_{\boldsymbol{\mu}=\boldsymbol{\mu}_0} + \left.\frac{\mathrm{d}\hat{\mathbf{H}}_{\mathrm{sd}}}{\mathrm{d}\mu_1}\right|_{\boldsymbol{\mu}=\boldsymbol{\mu}_0} \nu_1 + \left.\frac{\mathrm{d}\hat{\mathbf{H}}_{\mathrm{sd}}}{\mathrm{d}\mu_2}\right|_{\boldsymbol{\mu}=\boldsymbol{\mu}_0} \nu_2 + \cdots + \left.\frac{\mathrm{d}\hat{\mathbf{H}}_{\mathrm{sd}}}{\mathrm{d}\mu_d}\right|_{\boldsymbol{\mu}=\boldsymbol{\mu}_0} \nu_d + \text{H.O.T.} \tag{4}$$

where $\left.\frac{\mathrm{d}\hat{\mathbf{A}}_{\mathrm{sd}}}{\mathrm{d}\mu_i}\right|_{\boldsymbol{\mu}=\boldsymbol{\mu}_0}$ and $\left.\frac{\mathrm{d}\hat{\mathbf{H}}_{\mathrm{sd}}}{\mathrm{d}\mu_i}\right|_{\boldsymbol{\mu}=\boldsymbol{\mu}_0}$ denote component-wise derivatives for $i = 1, 2, \ldots, d$, and H.O.T. denote the respective higher-order terms. Truncating the H.O.T. in (3) and (4) and plugging the corresponding linear approximations into (2), we obtain the following quadratic-bilinear (QB) ROM:

$$\frac{\mathrm{d}\hat{\mathbf{q}}}{\mathrm{d}t}(t;\boldsymbol{\mu}) = \left(\hat{\mathbf{A}}_{\mathrm{sd},0} + \sum_{i=1}^{d} \nu_i \hat{\mathbf{A}}_{\mathrm{sd},i}\right) \hat{\mathbf{q}}(t;\boldsymbol{\mu}) + \left(\hat{\mathbf{H}}_{\mathrm{sd},0} + \sum_{i=1}^{d} \nu_i \hat{\mathbf{H}}_{\mathrm{sd},i}\right) \left(\hat{\mathbf{q}}(t;\boldsymbol{\mu}) \otimes \hat{\mathbf{q}}(t;\boldsymbol{\mu})\right), \tag{5}$$

where we denote

$$\hat{\mathbf{A}}_{\mathrm{sd},0} = \hat{\mathbf{A}}_{\mathrm{sd}}|_{\boldsymbol{\mu}=\boldsymbol{\mu}_0}, \quad \hat{\mathbf{H}}_{\mathrm{sd},0} = \hat{\mathbf{H}}_{\mathrm{sd}}|_{\boldsymbol{\mu}=\boldsymbol{\mu}_0} \quad \text{and} \quad \hat{\mathbf{A}}_{\mathrm{sd},i} = \left.\frac{\mathrm{d}\hat{\mathbf{A}}_{\mathrm{sd}}}{\mathrm{d}\mu_i}\right|_{\boldsymbol{\mu}=\boldsymbol{\mu}_0}, \quad \hat{\mathbf{H}}_{\mathrm{sd},i} = \left.\frac{\mathrm{d}\hat{\mathbf{H}}_{\mathrm{sd}}}{\mathrm{d}\mu_i}\right|_{\boldsymbol{\mu}=\boldsymbol{\mu}_0} \quad \text{for} \quad i = 1, 2, \ldots, d.$$

Note that these reduced operators do not depend on the parameters $\boldsymbol{\mu}$; the parametric dependence of the ROM comes in through the ν_i terms in (5). For more details on QB ROMs, see, e.g., [18–20].

Eq. (5) defines the form of the parametric ROM we seek to learn from snapshot data. OpInf is then used to find the reduced operators $\hat{\mathbf{A}}_{\mathrm{sd},i} \in \mathbb{R}^{r\times r}$ and $\hat{\mathbf{H}}_{\mathrm{sd},i} \in \mathbb{R}^{r\times r^2}$ for $i = 0, 1, \ldots, d$. This formulation follows the original OpInf formulation in [11] in targeting semi-discrete (time-continuous) ROMs. This requires the time derivatives of the projected snapshots, $\frac{d}{dt}\hat{\mathbf{Q}}$. When the time derivatives are not provided by the underlying simulation code, they need to be estimated numerically via, e.g., finite differences, from the values of $\hat{\mathbf{Q}}$. This poses a challenge when the available data set is down-sampled, which is typically the case in large-scale unsteady problems where it is prohibitive to store all time instants from the underlying high-fidelity simulation, since it becomes difficult to accurately approximate $\frac{d}{dt}\hat{\mathbf{Q}}$. An inaccurate approximation introduces noise in the OpInf least-squares learning problem which in turn leads to an inaccurate ROM. In this work, we therefore modify our implementation to learn the reduced operators of the fully discrete QB ROM

$$\hat{\mathbf{q}}[k+1] = \left(\hat{\mathbf{A}}_{\mathrm{fd},0} + \sum_{i=1}^{d} \nu_i \hat{\mathbf{A}}_{\mathrm{fd},i}\right) \hat{\mathbf{q}}[k] + \left(\hat{\mathbf{H}}_{\mathrm{fd},0} + \sum_{i=1}^{d} \nu_i \hat{\mathbf{H}}_{\mathrm{fd},i}\right) \left(\hat{\mathbf{q}}[k] \otimes \hat{\mathbf{q}}[k]\right), \tag{6}$$

where $\hat{\mathbf{q}}[k]$ now denotes the state of the fully discrete ROM at timestep k, with $\hat{\mathbf{q}}[1] = \hat{\mathbf{q}}_{\mathrm{init}}$ and $k = 1, 2, \ldots, n_t - 1$. Note that in (6) we have omitted the parametric dependence of the state $\hat{\mathbf{q}}$ for notational clarity.

The task now is to learn the operators of the fully discrete ROM, $\hat{\mathbf{A}}_{\mathrm{fd},i} \in \mathbb{R}^{r\times r}$ and $\hat{\mathbf{H}}_{\mathrm{fd},i} \in \mathbb{R}^{r\times r^2}$ for $i = 0, 1, \ldots, d$, where the subscript fd denotes *fully discrete*. We achieve this by splitting the projected data matrix $\hat{\mathbf{Q}}$ into two matrices:

$$\hat{\mathbf{Q}}_0 = \begin{bmatrix}\hat{\mathbf{Q}}_0(\boldsymbol{\mu}_1) & \hat{\mathbf{Q}}_0(\boldsymbol{\mu}_2) & \cdots & \hat{\mathbf{Q}}_0(\boldsymbol{\mu}_m)\end{bmatrix} \in \mathbb{R}^{r\times m(n_t-1)} \quad \text{and} \quad \hat{\mathbf{R}} = \begin{bmatrix}\hat{\mathbf{R}}(\boldsymbol{\mu}_1) & \hat{\mathbf{R}}(\boldsymbol{\mu}_2) & \cdots & \hat{\mathbf{R}}(\boldsymbol{\mu}_m)\end{bmatrix} \in \mathbb{R}^{r\times m(n_t-1)},$$

with $\hat{\mathbf{Q}}_0(\boldsymbol{\mu}_j) = \left[\hat{\mathbf{q}}_1(\boldsymbol{\mu}_j), \hat{\mathbf{q}}_2(\boldsymbol{\mu}_j), \ldots, \hat{\mathbf{q}}_{n_t-1}(\boldsymbol{\mu}_j)\right]^\top \in \mathbb{R}^{r\times n_t-1}$ and $\hat{\mathbf{R}}(\boldsymbol{\mu}_j) = \left[\hat{\mathbf{q}}_2(\boldsymbol{\mu}_j), \hat{\mathbf{q}}_3(\boldsymbol{\mu}_j), \ldots, \hat{\mathbf{q}}_{n_t}(\boldsymbol{\mu}_j)\right]^\top \in \mathbb{R}^{r\times n_t-1}$. Let

$$\hat{\mathbf{Q}}_i = \begin{bmatrix}\hat{\mathbf{Q}}_0(\boldsymbol{\mu}_1)\nu_{i1} & \hat{\mathbf{Q}}_0(\boldsymbol{\mu}_2)\nu_{i2} & \cdots & \hat{\mathbf{Q}}_0(\boldsymbol{\mu}_m)\nu_{im}\end{bmatrix} \in \mathbb{R}^{r\times m(n_t-1)},$$

where ν_{ij} denotes the ith component of $\boldsymbol{\nu}_j = \boldsymbol{\mu}_j - \boldsymbol{\mu}_0$ for $i = 1, 2, \ldots, d$ and $j = 1, 2, \ldots, m$, and let

$$\hat{\mathbf{P}}_0 = \hat{\mathbf{Q}}_0 \otimes \hat{\mathbf{Q}}_0 \quad \text{and} \quad \hat{\mathbf{P}}_i = \begin{bmatrix}\left(\hat{\mathbf{Q}}_0(\boldsymbol{\mu}_1) \otimes \hat{\mathbf{Q}}_0(\boldsymbol{\mu}_1)\right)\nu_{i1} & \left(\hat{\mathbf{Q}}_0(\boldsymbol{\mu}_2) \otimes \hat{\mathbf{Q}}_0(\boldsymbol{\mu}_2)\right)\nu_{i2} & \cdots & \left(\hat{\mathbf{Q}}_0(\boldsymbol{\mu}_m) \otimes \hat{\mathbf{Q}}_0(\boldsymbol{\mu}_m)\right)\nu_{im}\end{bmatrix},$$

where $\hat{\mathbf{P}}_i \in \mathbb{R}^{r^2\times m(n_t-1)}$ for $i = 0, 1, \ldots, d$. The following linear least-squares problem must be solved

$$\underset{\hat{\mathbf{O}}_{\mathrm{fd}}\in\mathbb{R}^{r\times d(r+r^2)}}{\operatorname{argmin}} \left\|\hat{\mathbf{D}}\hat{\mathbf{O}}_{\mathrm{fd}}^\top - \hat{\mathbf{R}}^\top\right\|_F^2 + \lambda_1 \left\|\hat{\mathbf{A}}_{\mathrm{fd}}\right\|_F^2 + \lambda_2 \left\|\hat{\mathbf{H}}_{\mathrm{fd}}\right\|_F^2, \tag{7}$$

where

$$\hat{\mathbf{O}}_{\mathrm{fd}} = \begin{bmatrix}\hat{\mathbf{A}}_{\mathrm{fd}} & \hat{\mathbf{H}}_{\mathrm{fd}}\end{bmatrix} \in \mathbb{R}^{r\times d(r+r^2)} \qquad \text{(unknown operators)}$$

$$\hat{\mathbf{D}} = \begin{bmatrix}\hat{\mathbf{Q}}^\top & \hat{\mathbf{P}}^\top\end{bmatrix} \in \mathbb{R}^{m(n_t-1)\times d(r+r^2)} \qquad \text{(known data)},$$

Distribution Statement A: Approved for Public Release; Distribution is Unlimited. PA# AFRL-2022-5626

where we denote

$$\hat{\mathbf{A}}_{\text{fd}} = \begin{bmatrix} \hat{\mathbf{A}}_{\text{fd},0} & \hat{\mathbf{A}}_{\text{fd},1} & \cdots & \hat{\mathbf{A}}_{\text{fd},d} \end{bmatrix}$$
$$\hat{\mathbf{H}}_{\text{fd}} = \begin{bmatrix} \hat{\mathbf{H}}_{\text{fd},0} & \hat{\mathbf{H}}_{\text{fd},1} & \cdots & \hat{\mathbf{H}}_{\text{fd},d} \end{bmatrix}$$
$$\hat{\mathbf{Q}}^{\top} = \begin{bmatrix} \hat{\mathbf{Q}}_0^{\top} & \hat{\mathbf{Q}}_1^{\top} & \cdots & \hat{\mathbf{Q}}_d^{\top} \end{bmatrix}$$
$$\hat{\mathbf{P}}^{\top} = \begin{bmatrix} \hat{\mathbf{P}}_0^{\top} & \hat{\mathbf{P}}_1^{\top} & \cdots & \hat{\mathbf{P}}_d^{\top} \end{bmatrix}.$$

This least squares problem uses Tikhonov regularization to avoid overfitting and to account for model misspecification, where $\lambda_1, \lambda_2 \in \mathbb{R}$ are scalar regularization hyperparameters [14]. Note that for a linear system, the discrete OpInf formulation is equivalent to (parametric) dynamic mode decomposition (DMD) [21, 22].

III. Parametric large-scale rotating detonation rocket engine simulations

A. Problem setup for high-fidelity large-eddy simulation

The full-order RDRE data used in our numerical experiments comes from a set of implicit LES done using the AHFM (ALREST High-Fidelity Modeling) code for previous versions of the Air Force Research Lab (AFRL) RDRE. Literature on the AFRL RDRE [17, 23] shows more details of the code, typical computational setup, and detailed analysis of previous results. The physics of the problem are modeled using the reactive, viscous Navier-Stokes equations coupled with a skeletal chemistry-mechanism (FFCMy-12) based on the FFCM model [24] or a modified Westbrook-Dryer mechanism [25]. This version of the AFRL RDRE uses gaseous methane and oxygen which are injected through 72 doublet-impinger pairs. The computational mesh-size is around 136 million cells for the complete RDRE. These simulations are computationally very expensive, where a typical simulation running on 16,060 cores on a supercomputer requires a total of six million CPU-hours for 2 ms of simulated physical time.

This work focuses on constructing parametric ROMs for the solutions within the full 360-degree RDRE combustion chamber. The ROM domain is slightly smaller in each dimension than the computational fluid dynamics (CFD) domain. Depicted in Figure 1, the ROM domain spans from 0.05 to 76.15 mm in the x direction, spans from -37.5 to 37.5 mm in both y and z directions, and has a fixed channel height of 4.44 mm throughout. The original simulation data has been interpolated onto a grid domain comprising

$$n_x = 4,204,200$$

spatial degrees of freedom, with clustering of grid points at mid channel and closer toward the injector plane.

B. Parameter description

We have available two data sets corresponding to two injector designs. Both designs have 72 discrete injector-pairs. These two designs are characterized by different oxidizer-to-fuel area ratios and impingement-cavity recess distances. The parametric variations are concerned with the flow conditions (mass flow-rate, $\dot{m}[\text{kg/s}]$, and equivalence ratio, Φ) of the particular case. As discussed by Bykovskii et al. [1] and Bennewitz et al. [26], the mass flow-rate and equivalence ratio control RDRE dynamical behavior including the number of waves, presence of counter-propagating waves, and so forth. Figure 1 shows iso-surfaces of the interpolated pressure-field for the first injector design at nominal conditions, for which there are five co-rotating detonation waves. These variations are characterized in our model using a scalar parameter $\mu \in \mathbb{R}$ that depends on a weighted combination of normalized mass flow-rate and equivalence ratio:

$$\mu = \frac{\dot{m}}{\dot{m}_0} + \frac{\Phi}{\Phi_0}, \tag{8}$$

where the normalization is done with respect to their respective maximum values $\dot{m}_0$ and Φ_0 across all cases. Therefore, the parametric dimension is $d = 1$. Given the complexity of these problems, a scenario with a single parameter represents a good starting point which can offer valuable insights regarding the potential of the discrete OpInf procedure summarized in Section II.B to construct accurate and predictive parametric ROMs for large-scale RDRE combustion chambers. In our future research, we will consider parametric settings in which variations in $\dot{m}$ and Φ will be considered separately. Moreover, we also aim to consider variations in parameters characterizing the geometry.

Distribution Statement A: Approved for Public Release; Distribution is Unlimited. PA# AFRL-2022-5626

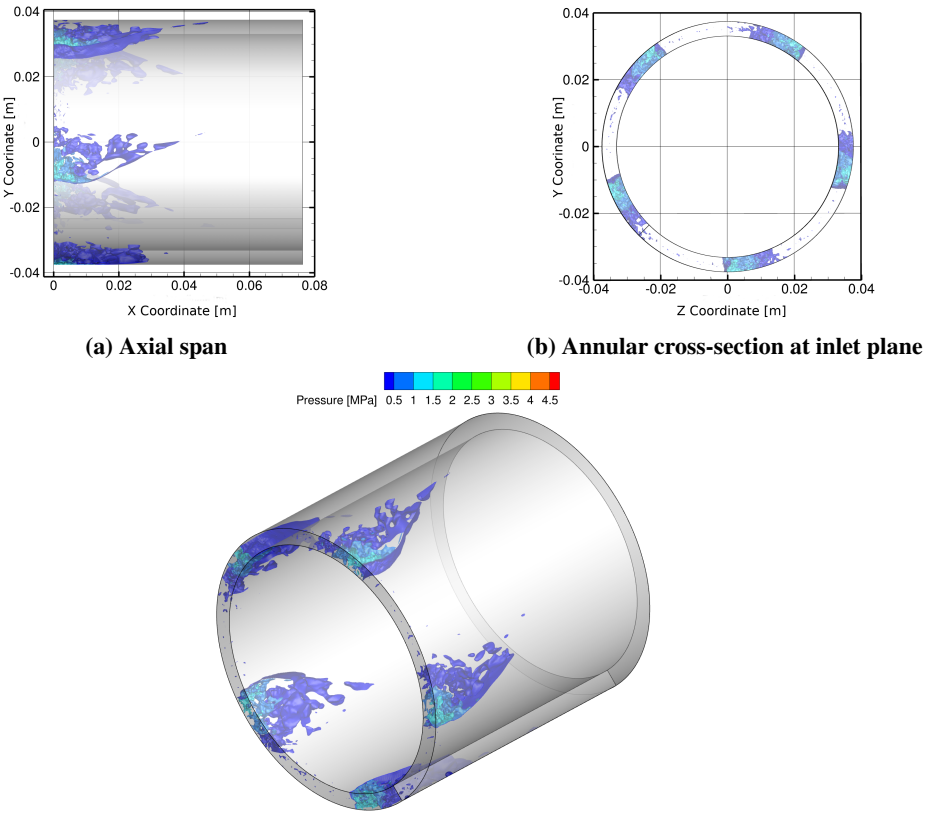

(a) Axial span

(b) Annular cross-section at inlet plane

(c) Isometric view

Fig. 1 Pressure iso-surfaces in the combustion chamber for first injector design at nominal conditions.

IV. Numerical results and discussion

We perform two numerical experiments in which we construct parametric ROMs via OpInf for RDRE combustion chambers. Section IV.A investigates the prediction capability of parametric OpInf ROMs at instances outside of the training set. Section IV.B assess the prediction capability of parametric OpInf ROMs beyond the training horizon.

A. First injector design: parametric predictions outside of the training set

For the first injector design, we have LES data for three parameter instances: $\mu_1 = 1.41$, $\mu_2 = 1.73$, and $\mu_3 = 1.55$. Table 1 shows the corresponding flow condition (second column), mass-flow rate (third column), equivalence ratio (fourth column), number of dominant waves (seventh column), and number of secondary waves (last column). Since $\mu_1 = 1.41$ corresponds to nominal flow, it is used as the nominal value in the Taylor series expansions (3) and (4). For each parameter instance, we have $n_t = 100$ down-sampled snapshots from the high-fidelity simulation, which correspond to roughly 0.25 ms of physical time. The corresponding time domain and number of wave periods are shown in the fifth and sixth columns in Table 1. The average time step between the down-sampled snapshots is $\Delta t = 2.5 \times 10^{-3}$ ms. All dominant waves are co-rotating. The first (corresponding to nominal flow) and third (corresponding to high mass-flow-rate flow) parameter instances have five corresponding co-rotating dominant waves and no secondary waves. In contrast, the second instance, i.e., the high equivalence-ratio case, is characterized by six dominant co-rotating waves and eight secondary counter-rotating waves. These heterogeneous and complex dynamics, as well as the sparsity of the available data sets make the construction of accurate and predictive data-driven ROMs very challenging.

Following the work in [13–16], we build the ROMs using the specific volume flow variables (specific volume, pressure and the three velocity components), species mass fractions and temperature. We transform the data snapshots to represent the following $n_s = 8$ state variables:

$$q = [1/\rho \;\; p \;\; v_x \;\; v_y \;\; v_z \;\; w_{\mathrm{CH_4}} \;\; w_{\mathrm{O_2}} \;\; T]^\top, \tag{9}$$

Distribution Statement A: Approved for Public Release; Distribution is Unlimited. PA# AFRL-2022-5626

μ	Flow Condition	$\dot{m}$ (kg/s)	Φ	Time Interval	Periods	Dominant Waves	Secondary Waves
$\mu_1 = 1.41$	nominal	0.267	1.16	[3.7525 ms, 4.0000 ms]	1.97	5	0
$\mu_2 = 1.73$	high Φ	0.266	1.71	[1.8425 ms, 2.0900 ms]	1.64	6	8
$\mu_3 = 1.55$	high $\dot{m}$	0.333	1.09	[3.7525 ms, 4.0000 ms]	1.97	5	0

Table 1 First injector design: summary of the three parameter instances used in the numerical experiments.

where ρ is density, p is pressure, v_x, v_y, v_z are the three velocity components, w_{CH_4} and w_{O_2} are the species mass fractions of fuel (CH_4) and oxidizer (O_2), and T is temperature. This representation makes most terms in the underlying model (cf. Section III.A) linear or quadratic in the above state variables. The total number of spatial degrees of freedom for each parameter instance is thus $n = n_s \times n_x = 8 \times 4,204,200 = 33,633,600$. Note that the eight state variables have significantly different scales. For example, the pressure scale is of order 10^5 to 10^6 Pa, whereas the species mass fractions are in $[0, 1]$. We therefore center and scale the snapshot data variable-by-variable prior to performing OpInf: each state variable is first centered around the mean field (over the training data) in that variable, and then scaled by the maximum absolute value of that variable so that the values for each state variable do not exceed $[-1, 1]$.

We use high-fidelity simulation data corresponding to μ_1 and μ_2 to train a parametric QB OpInf ROM (6) and we use the data corresponding to μ_3 for predictions outside of the training set. We therefore have 200 training snapshots in total, i.e., the snapshot matrix $\mathbf{Q} \in \mathbb{R}^{33,633,600\times 200}$.

Figure 2 plots the normalized singular values (normalized with respect to the first singular value) on the left and the POD retained energy corresponding to the centered and scaled training data set on the right. Note the slow decay of the singular values, which is due to the complex and transport-dominated nature of the dynamics of these problems. For example, to retain 95% of the total energy, $r = 173$ modes are needed. The small size of the training set (200 snapshots) limits the maximum reduced dimension of a parametric QB OpInf reduced model (6) to $r = 12$, because this sets the maximum number of operator coefficients that can be inferred via the OpInf regression problem (7). This reduced dimension retains 43.99% of the total energy.

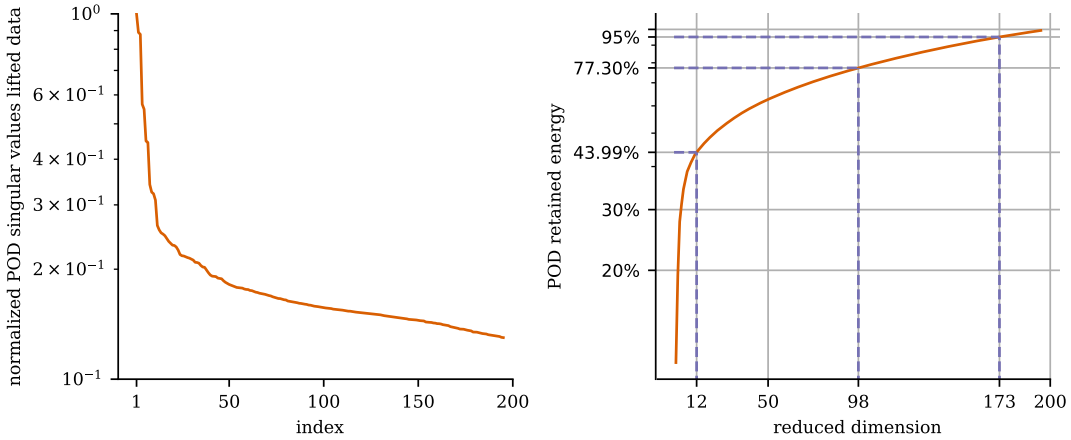

Fig. 2 First injector design with 200 training snapshots: normalized singular values (left) and POD retained energy (right).

In our numerical experiments, we consider parametric QB OpInf reduced models (6) with reduced dimension $r = 12$. Moreover, since the available training data is small in size, we additionally consider a linear parametric ROM by neglecting the quadratic and quadratic-bilinear terms in (6), which amounts to a DMD ROM [21, 22]. Such an approach is motivated by Koopman operator theory (see, e.g., [27, 28]). The maximum reduced dimension for the DMD ROM is $r = 98$, which we also employ in our experiments. This retains 77.30% of the total energy. In the following, we ascertain the prediction capabilities of both parametric DMD and QB OpInf ROMs for pressure, temperature, and fuel and oxidizer mass fractions. More specifically, the ROM solutions are used to extract the respective one-dimensional radial profiles at three representative locations close to the mid-channel, which will be compared with the corresponding

Distribution Statement A: Approved for Public Release; Distribution is Unlimited. PA# AFRL-2022-5626

profiles from the high-fidelity simulation. Axially, the first location is close to the injectors, the second location

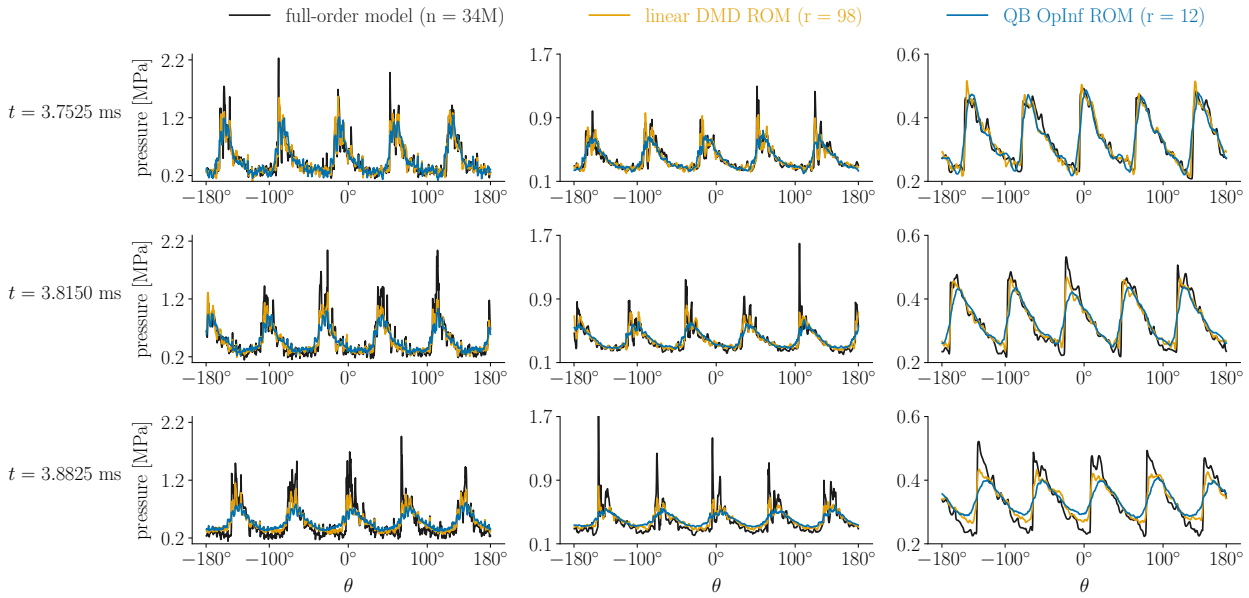

Fig. 3 First injector design: ROM approximate solutions of one-dimensional circumferential pressure profiles for $\mu_1 = 1.41$. The columns plot the results at three locations close to the mid-channel. The rows plot the results at three time instants within the first period.

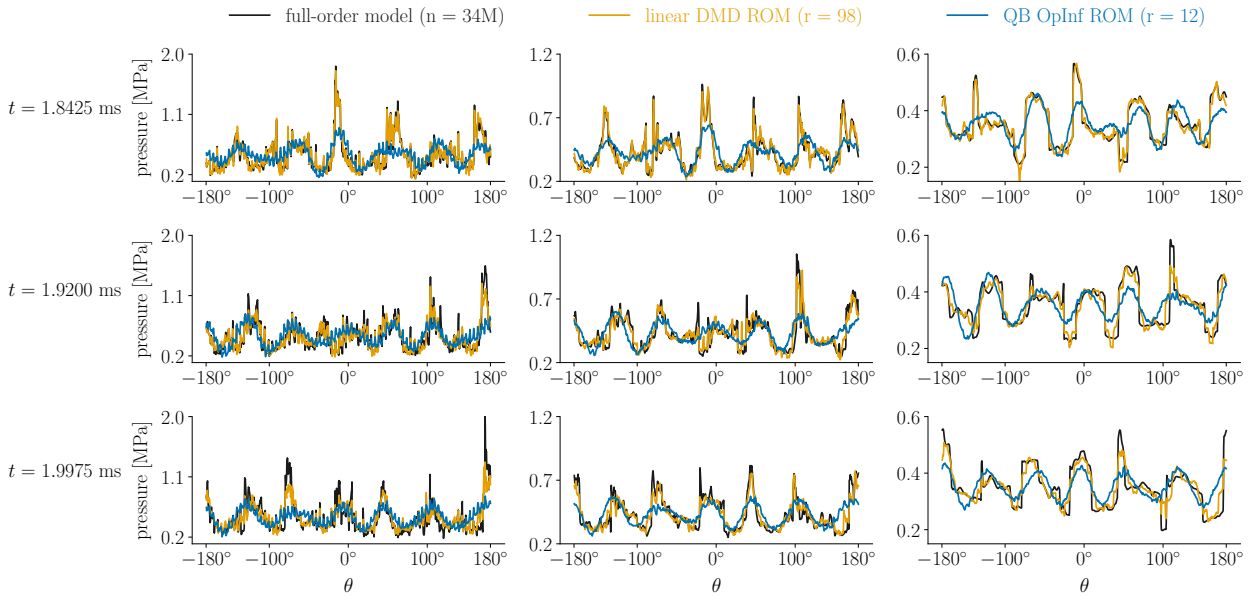

Fig. 4 First injector design: ROM approximate solutions of one-dimensional circumferential pressure profiles for $\mu_2 = 1.73$. The columns plot the results at three locations close to the mid-channel. The rows plot the results at three time instants within the first period.

is further way from the injectors but still within the detonation region, and the third location is downstream of the detonation zone.

We begin with the ROM approximate solutions for the two parameter instances used for training, $\mu_1 = 1.41$ and $\mu_2 = 1.73$. Figures 3 and 4 plot the respective one-dimensional pressure profiles. In both figures, the pressure profiles at the first location are plotted in the first column, the profiles at the second location in the second column, and the pressure

Distribution Statement A: Approved for Public Release; Distribution is Unlimited. PA# AFRL-2022-5626

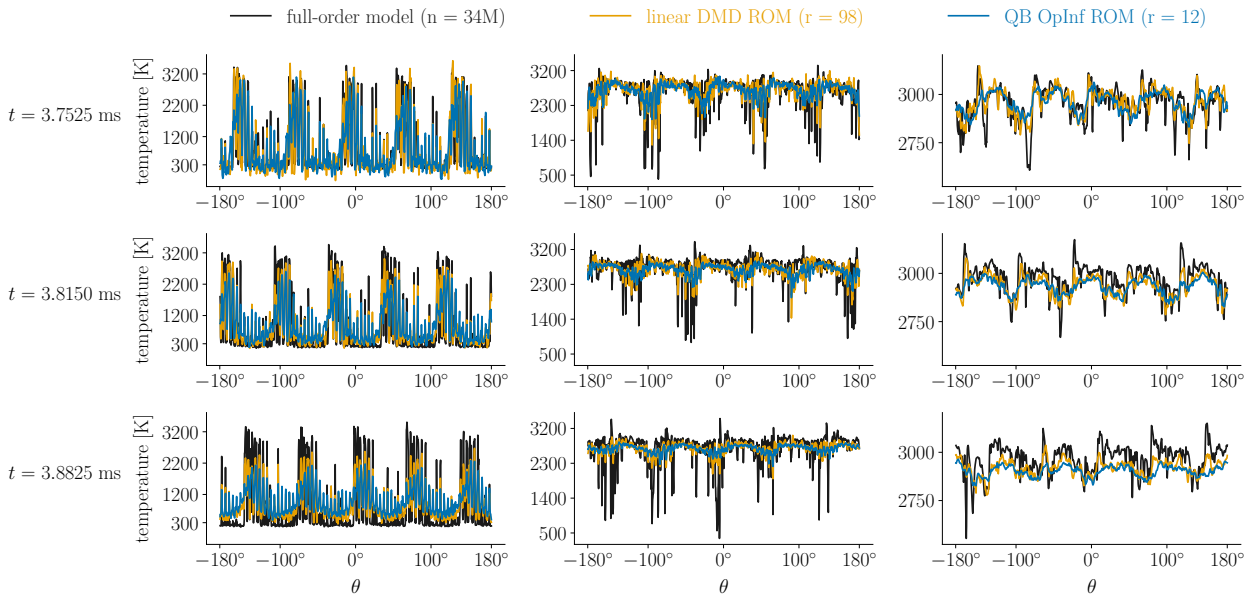

Fig. 5 First injector design: ROM approximate solutions of one-dimensional circumferential temperature profiles for $\mu_1 = 1.41$. The columns plot the results at three locations close to the mid-channel. The rows plot the results at three time instants within the first period.

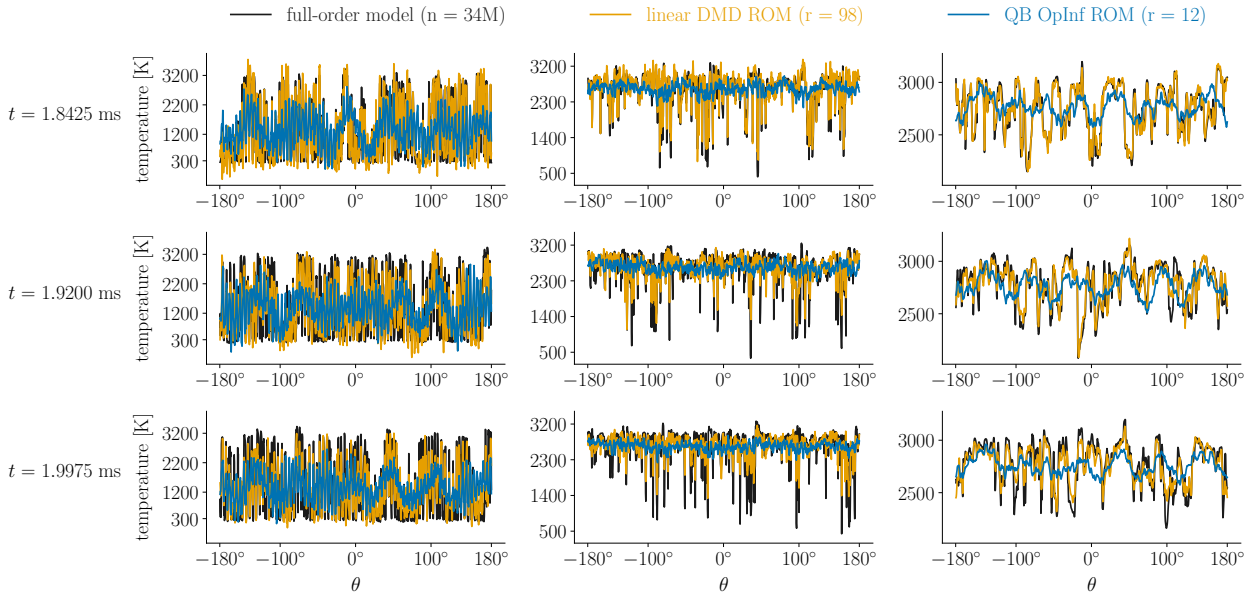

Fig. 6 First injector design: ROM approximate solutions of one-dimensional circumferential temperature profiles for $\mu_2 = 1.73$. The columns plot the results at three locations close to the mid-channel. The rows plot the results at three time instants within the first period.

profiles corresponding to the third location are visualized in the third column. The rows in Figure 3 plot the results at three time instants within the first wave period for μ_1: $t = 3.7525$ ms in the first row (first time instant), $t = 3.8148$ ms (25th time instant) in the second row, and $t = 3.8823$ ms (52nd time instant) in the third row. Both ROMs accurately approximate the frequency of the pressure waves at all three locations. However, the DMD ROM approximates the amplitudes more accurately than the QB OpInf ROM. The rows in Figure 4 plot the results at three time instants within the first wave period for μ_2: $t = 1.8425$ ms in the first row (first time instant), $t = 1.9200$ ms (31st time instant) in the second row, and $t = 1.9975$ ms (62nd time instant) in the third row. Recall that the dynamics corresponding to this

Distribution Statement A: Approved for Public Release; Distribution is Unlimited. PA# AFRL-2022-5626

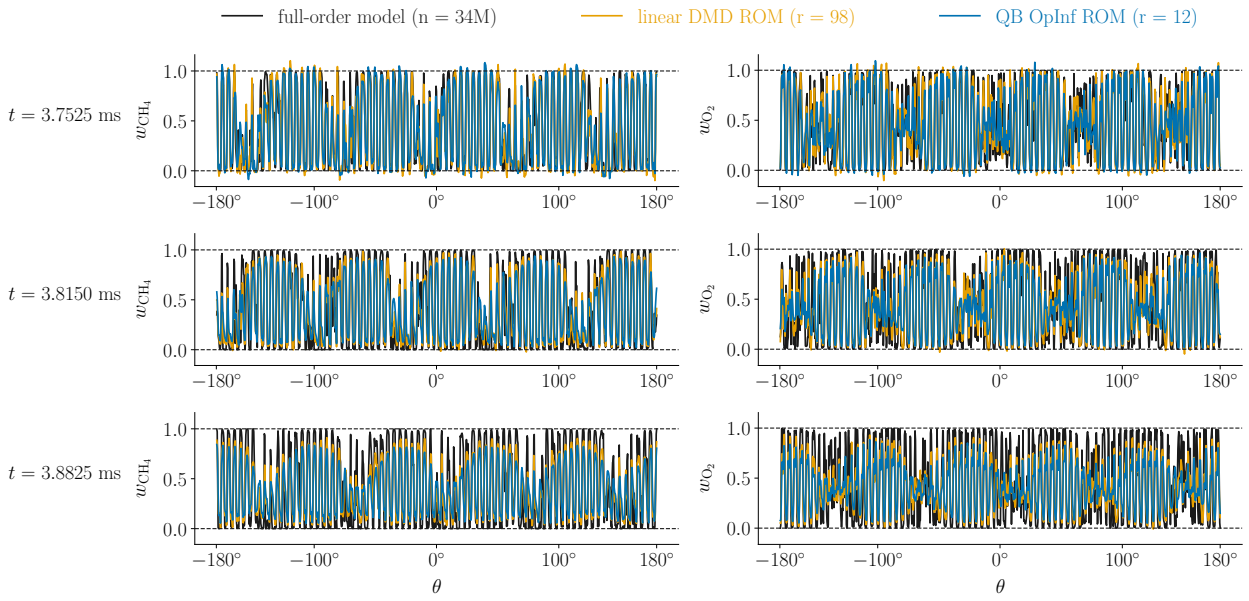

Fig. 7 First injector design: ROM approximate solutions of one-dimensional circumferential fuel (left column) and oxidizer (right column) mass fraction profiles close to the injectors, at mid-channel, for $\mu_1 = 1.41$. The rows plot the results at three time instants within the first period.

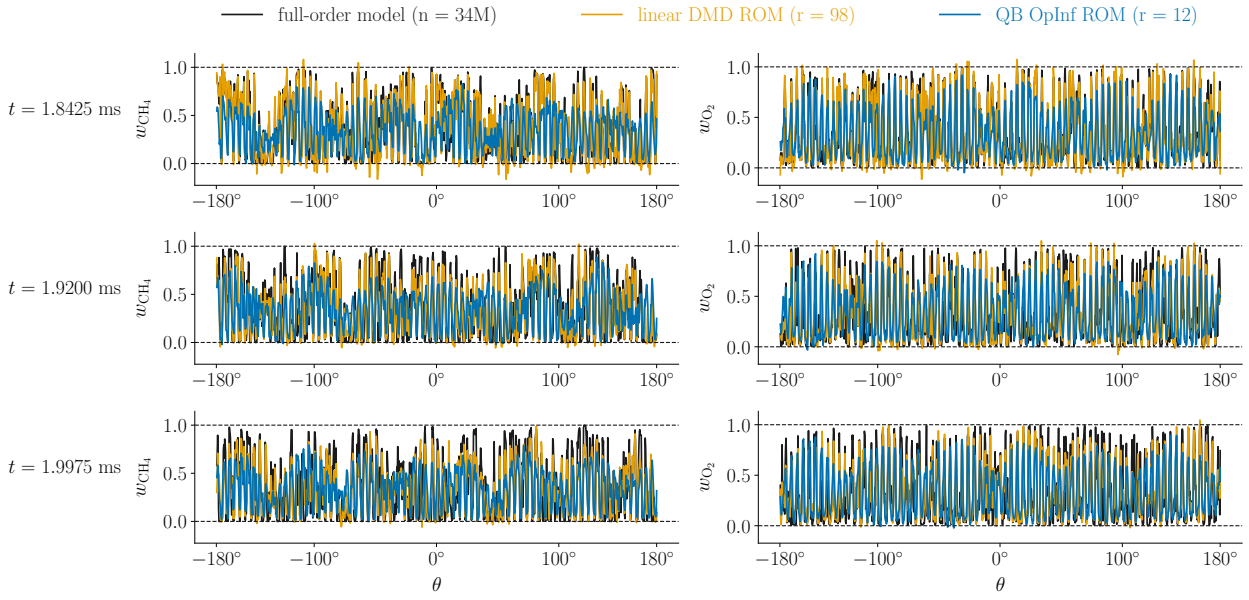

Fig. 8 First injector design: ROM approximate solutions of one-dimensional circumferential fuel (left column) and oxidizer (right column) mass fraction profiles close to the injectors, at mid-channel, for $\mu_2 = 1.73$. The rows plot the results at three time instants within the first period.

parameter instance are the most complex, being characterized by six dominant co-rotating waves and eight secondary counter-propagating waves (cf. Table 1). Therefore, here we observe a larger discrepancy between the approximate solutions of the two ROMs: even though the QB OpInf ROM approximates the frequency of the pressure waves fairly well, it is less accurate than the DMD ROM. The DMD ROM, in contrast, accurately approximates both the frequency and amplitude of the pressure profiles.

Figures 5 and 6 plot the corresponding one-dimensional temperature profiles. Similarly to what was observed for pressure, the DMD ROM yields more accurate approximate solutions, especially for the second parameter instance

Distribution Statement A: Approved for Public Release; Distribution is Unlimited. PA# AFRL-2022-5626

μ_2, where we can see that the $r = 12$ POD basis vectors — which capture only low-frequencies — are insufficient for constructing an accurate parametric QB OpInf ROM.

Figures 7 and 8 plot the one-dimensional profiles for fuel (left column) and oxidizer (right column) mass fractions at the location axially close to the injectors. Since chemical species mass fractions must have values between zero and one, we additionally plot dashed lines at these values on the y-axes to visually verify whether the ROMs issue solutions below or above these thresholds. Besides a few solutions outside of $[0, 1]$ observed for the two mass fractions at the first time instant in both figures, the two ROMs yield accurate approximate solutions for both fuel and oxidizer.

We now present the ROM predictions for the third parameter instance outside of the training set, $\mu_3 = 1.55$. The results are visualized analogously to those for the two parameter instances used for training. Figure 9 plots the pressure predictions. The two ROMs accurately predict the frequency of the pressure profiles. The amplitudes, however, are

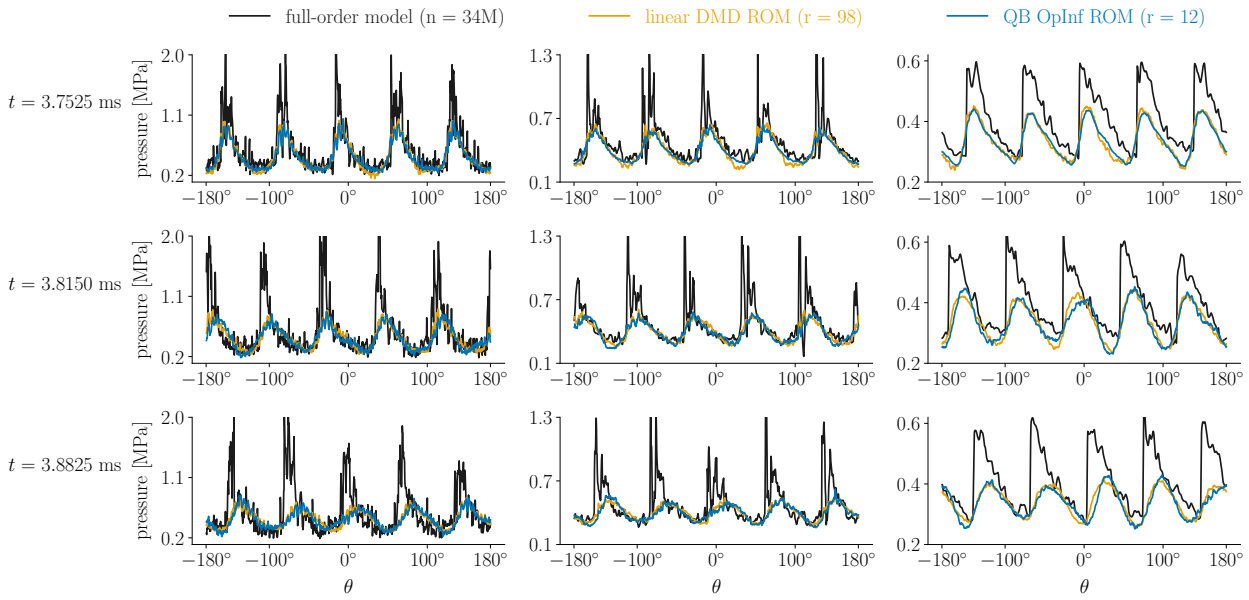

Fig. 9 First injector design: ROM predictions of one-dimensional circumferential pressure profiles for $\mu_3 = 1.55$ (outside of the training set). The columns plot the results at three locations close to the mid-channel. The rows plot the results at three time instants within the first period.

matched less accurately: neither ROM captures the peaks in the pressure profiles. Therefore, in contrast to what was observed for the training parameters, the two ROMs perform very similarly here. To better understand why, let us take a closer look at the pressure profile at the first time instant, i.e., the first row in Figure 9. The initial condition of the parametric ROMs stems from projecting the corresponding high-fidelity data onto the linear subspace spanned by the POD basis, obtained using the other two instances employed for training. The parametric ROMs then evolve this initial condition according to (6) or its linear (DMD) version, respectively. The reconstructions in the first row in Figure 9 thus indicate how well the reduced basis can represent the data corresponding to the third parameter. We see that the basis is not rich enough to accurately approximate the higher frequency components (corresponding to the smaller POD singular values). Nevertheless, given that the POD basis was constructed using data from only two parameter instances with heterogeneous dynamics, the ROMs perform quite well. We observe similar results for temperature in Figure 10. The fuel and oxidizer mass fractions are predicted accurately by both ROMs, as it can be seen in Figure 11.

B. Second injector design: predictions beyond the training horizon

For the second injector design, we have LES data for two parameter instances: $\mu_1 = 1.41$ and $\mu_2 = 1.60$. The corresponding flow condition (second column), mass-flow rate (third column), equivalence ratio (fourth column), number of dominant wave (seventh column), and number of secondary wave (last column) are respectively shown in Table 2. As for the first injector design, $\mu_1 = 1.41$ is used as the nominal value in the Taylor series approximations (3) and (4). We have 100 down-sampled snapshots for each parameter instance, which correspond to roughly 0.25 ms of physical time; the average time step between snapshots is $\Delta t = 2.5 \times 10^{-3}$ ms. The corresponding time domain and

Distribution Statement A: Approved for Public Release; Distribution is Unlimited. PA# AFRL-2022-5626

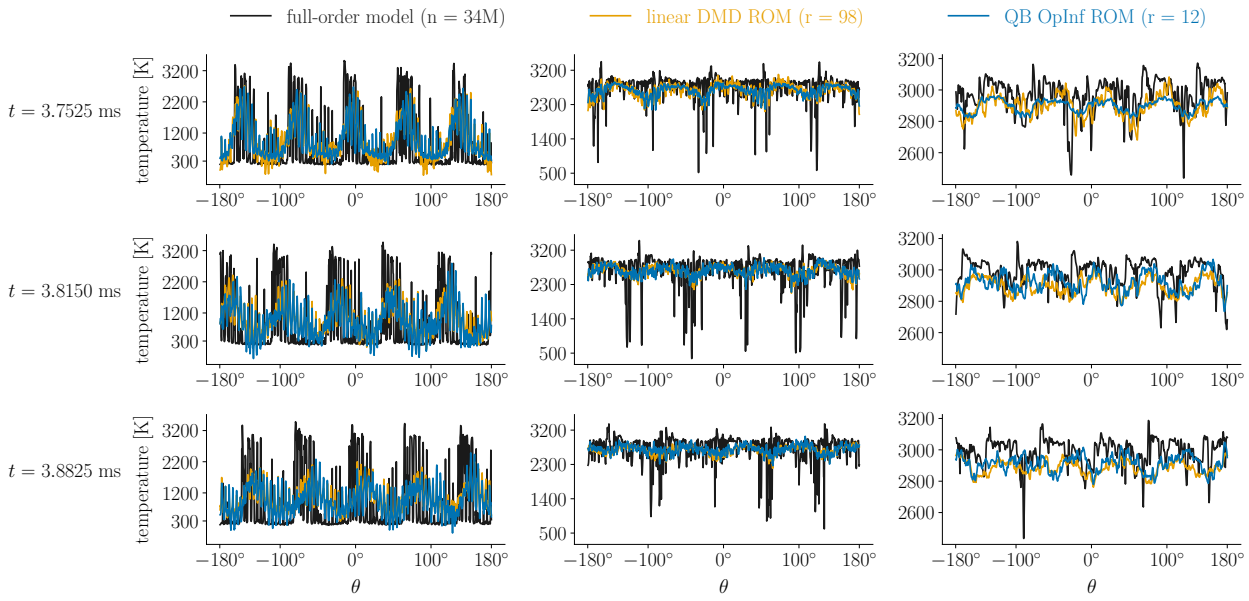

Fig. 10 First injector design: ROM predictions of one-dimensional circumferential temperature profiles for $\mu_3 = 1.55$ (outside of the training set). The columns plot the results at three locations close to the mid-channel. The rows plot the results at three time instants within the first period.

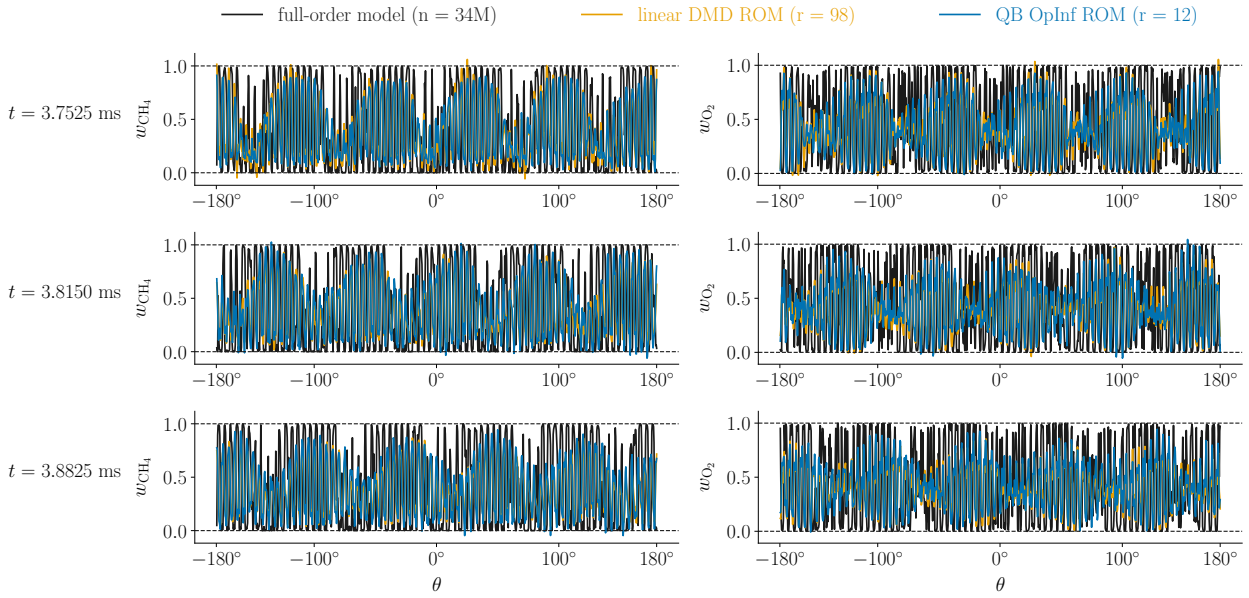

Fig. 11 First injector design: ROM predictions of one-dimensional circumferential fuel (left column) and oxidizer (right column) mass fraction profiles close to the injectors, at mid-channel, for $\mu_3 = 1.55$ (outside of the training set). The rows plot the results at three time instants within the first period.

number of wave periods are shown in the fifth and sixth columns in Table 2. Both parameter instances are characterized by two dominant co-rotating waves and no secondary waves. Since we have simulation data for only two instances, we will train ROMs using the first $n_t = 60$ snapshots from each parameter instance, which account for roughly one wave period, and use the ROMs for predictions for the remaining 40 time instants beyond the training horizon. Therefore, the snapshot matrix $\mathbf{Q} \in \mathbb{R}^{33,633,600\times120}$.

Figure 12 plots the normalized singular values on the left and the POD retained energy corresponding to the centered and scaled training data set on the right. The singular values decay slowly; to retain 95% of the total energy $r = 92$

Distribution Statement A: Approved for Public Release; Distribution is Unlimited. PA# AFRL-2022-5626

μ	Flow Condition	$\dot{m}$ (kg/s)	Φ	Time Interval	Periods	Dominant Waves	Secondary Waves
$\mu_1 = 1.41$	nominal	0.267	1.16	[4.9500 ms, 5.1975 ms]	1.97	2	0
$\mu_2 = 1.60$	high $\dot{m}$	0.349	1.10	[3.1250 ms, 3.3750 ms]	1.79	2	0

Table 2 Second injector design: summary of the two parameter instances used in the numerical experiments.

POD modes are needed. The small size of the training set (120 snapshots) limits the maximum reduced dimension of a parametric QB OpInf reduced model (6) to $r = 8$, which retains 53.23% of the total energy. As was done for the first injector design, we consider a DMD ROM here, too. The maximum reduced dimension for DMD is $r = 58$, which we also employ in our experiments. This retains 82.63% of the total energy.

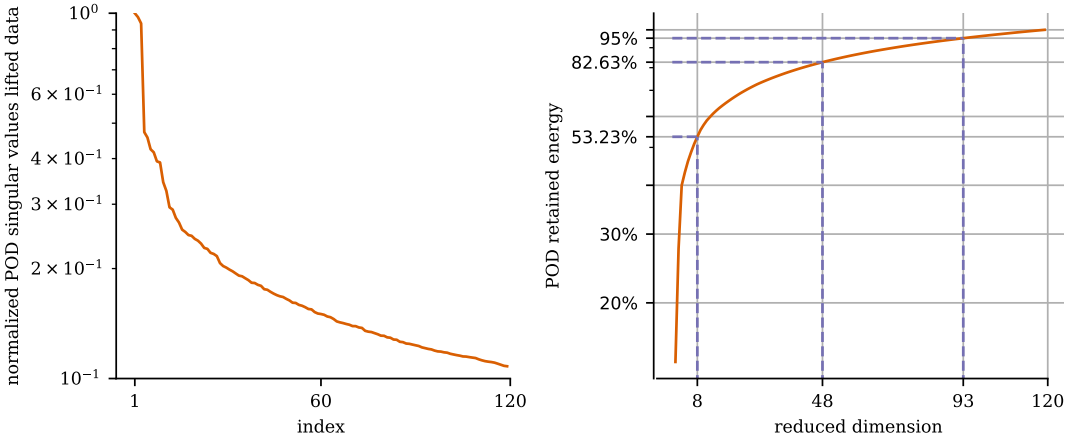

Fig. 12 Second injector design with 120 training snapshots: normalized singular values (left) and POD retained energy (right).

In the following, we ascertain the prediction capabilities beyond the training horizon of both DMD with reduced dimension $r = 58$ and the QB OpInf ROM with reduced dimension $r = 8$. Figures 13 and 14 depict the one-dimensional pressure profiles at the same three locations as for the first injector design. At each location, we depict profiles at four time instants (one per each row). The first row corresponds to the last time instant in the training domain ($t = 5.1000$ ms for μ_1 and $t = 3.2750$ ms for μ_2). The other three instants are in the prediction regime: the second row plots the first time instant in the prediction regime ($t = 5.1025$ ms for μ_1 and $t = 3.2775$ ms for μ_2), the third row plots the profiles for the 80th time instant (20th in the prediction regime, corresponding to $t = 5.1500$ ms for μ_1 and $t = 3.3250$ ms for μ_2), and the last row plots the results for the last time instant, i.e., $t = 5.1975$ ms for μ_1 and $t = 3.3750$ ms for μ_2. For an easier visualization, the results for the last time instant in the training domain are plotted using dashed lines. On the one hand, the results for μ_1 show that the DMD ROM predicts both the frequency and amplitude of the pressure waves more accurately that the QB OpInf ROM. Nevertheless, mismatches in the amplitudes can be observed, for example, for the second time instant in the prediction regime (third row). On the other hand, both ROMs predict both the frequency and amplitudes more accurately for μ_2.

Figures 15 and 16 plot the corresponding one-dimensional temperature profiles. Similarly to what was observed for pressure, here too both ROMs accurately match the trends of the temperature profiles, with DMD being more accurate in predicting the rapid temperature oscillations. Overall, given the rich structure of these profiles, the ROMs perform quite well.

Finally, Figures 17 and 18 depict the fuel and oxidizer mass fraction profiles at the location close to the injectors at the same four time instants as for pressure and temperature. The QB OpInf ROM matches the trends of the profiles but the eight POD modes used for training are not sufficient to capture the oscillating amplitudes as well. In contrast, DMD yields more accurate predictions for both μ_1 and μ_2.

Distribution Statement A: Approved for Public Release; Distribution is Unlimited. PA# AFRL-2022-5626

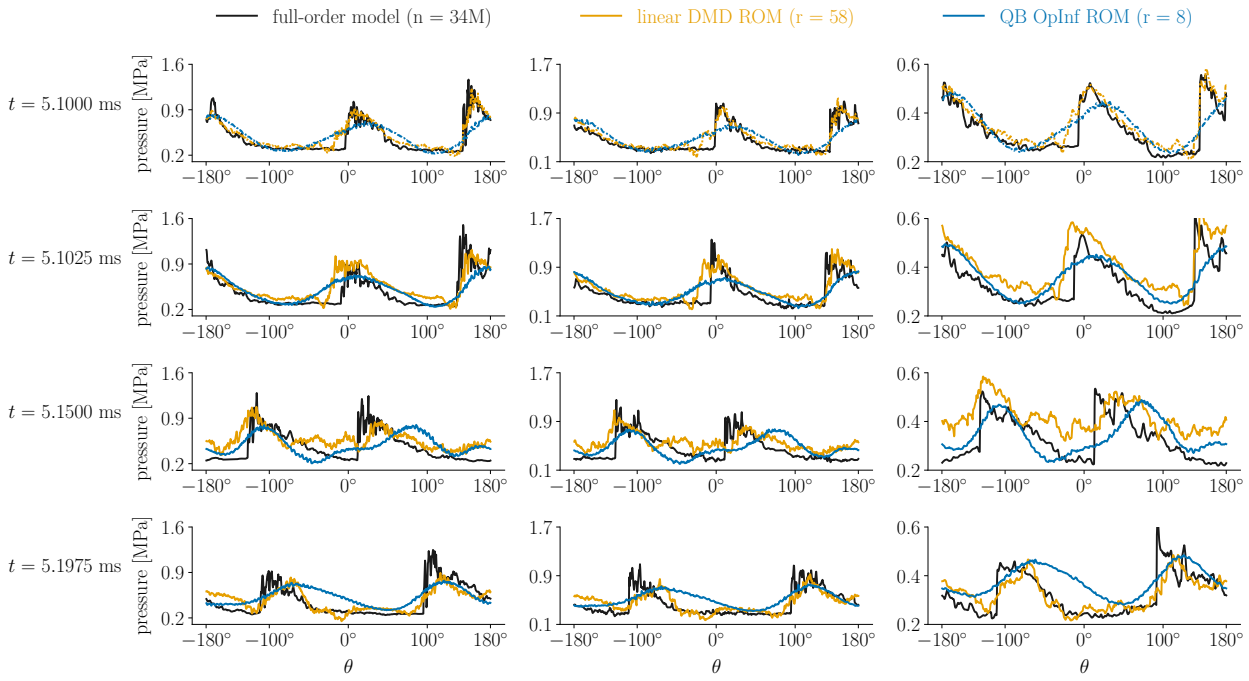

Fig. 13 Second injector design: ROM predictions of one-dimensional circumferential pressure profiles for $\mu_1 = 1.41$. The columns plot the results at three locations close to the mid-channel. The rows plot the results at four time instants: the last time instant in the training horizon (plotted using dashed lines) and three time instants in the prediction horizon.

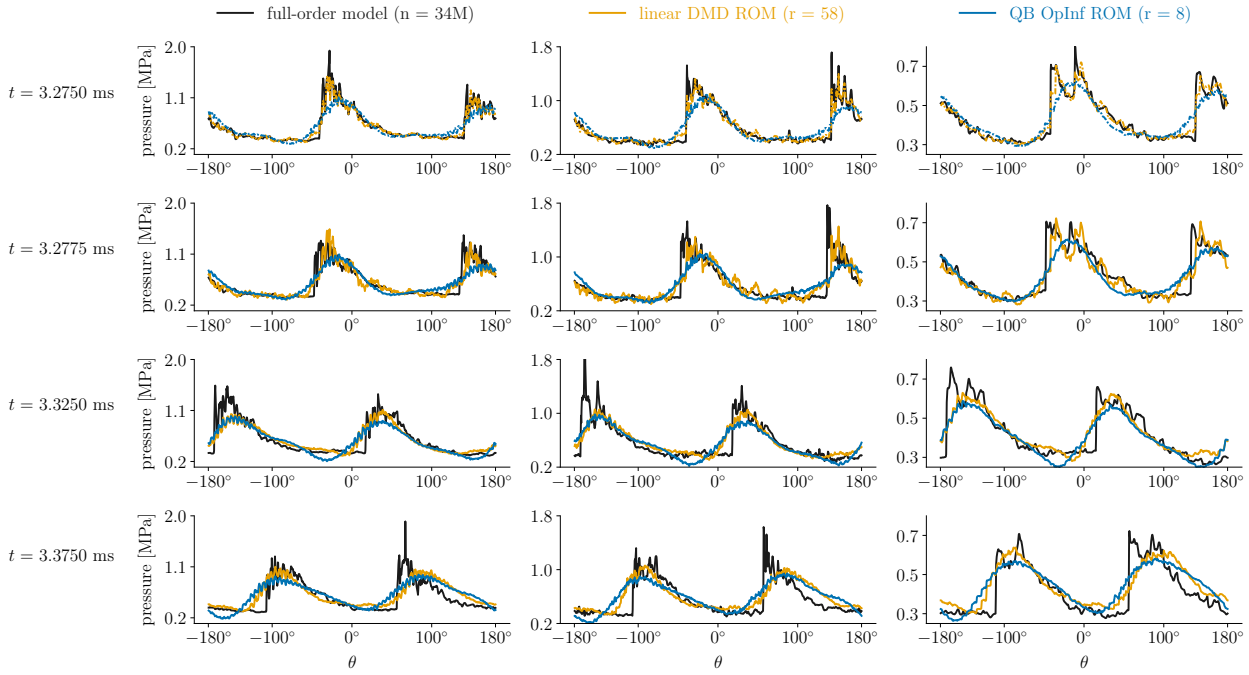

Fig. 14 Second injector design: ROM predictions of one-dimensional circumferential pressure profiles for $\mu_2 = 1.60$. The columns plot the results at three locations close to the mid-channel. The rows plot the results at four time instants: the last time instant in the training horizon (plotted using dashed lines) and three time instants in the prediction horizon.

Distribution Statement A: Approved for Public Release; Distribution is Unlimited. PA# AFRL-2022-5626

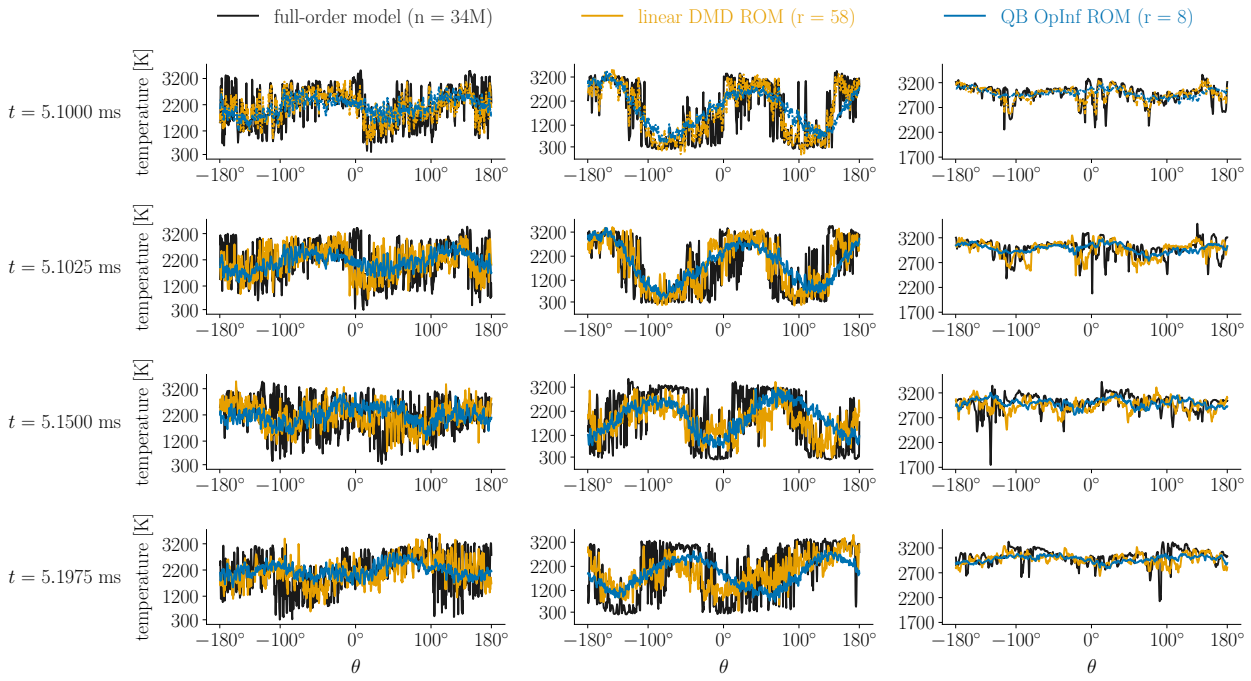

Fig. 15 Second injector design: ROM predictions of one-dimensional circumferential temperature profiles for $\mu_1 = 1.41$. The columns plot the results at three locations close to the mid-channel. The rows plot the results at four time instants: the last time instant in the training horizon (plotted using dashed lines) and three time instants in the prediction horizon.

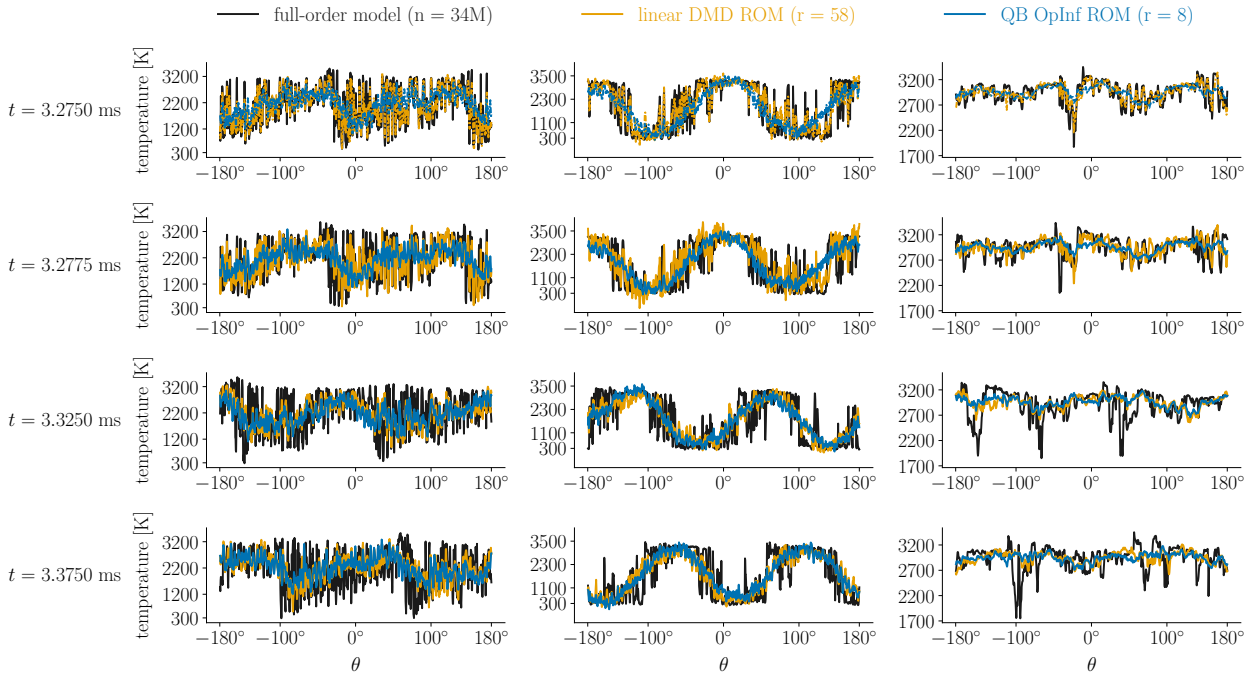

Fig. 16 Second injector design: ROM predictions of one-dimensional circumferential temperature profiles for $\mu_2 = 1.60$. The columns plot the results at three locations close to the mid-channel. The rows plot the results at four time instants: the last time instant in the training horizon (plotted using dashed lines) and three time instants in the prediction horizon.

Distribution Statement A: Approved for Public Release; Distribution is Unlimited. PA# AFRL-2022-5626

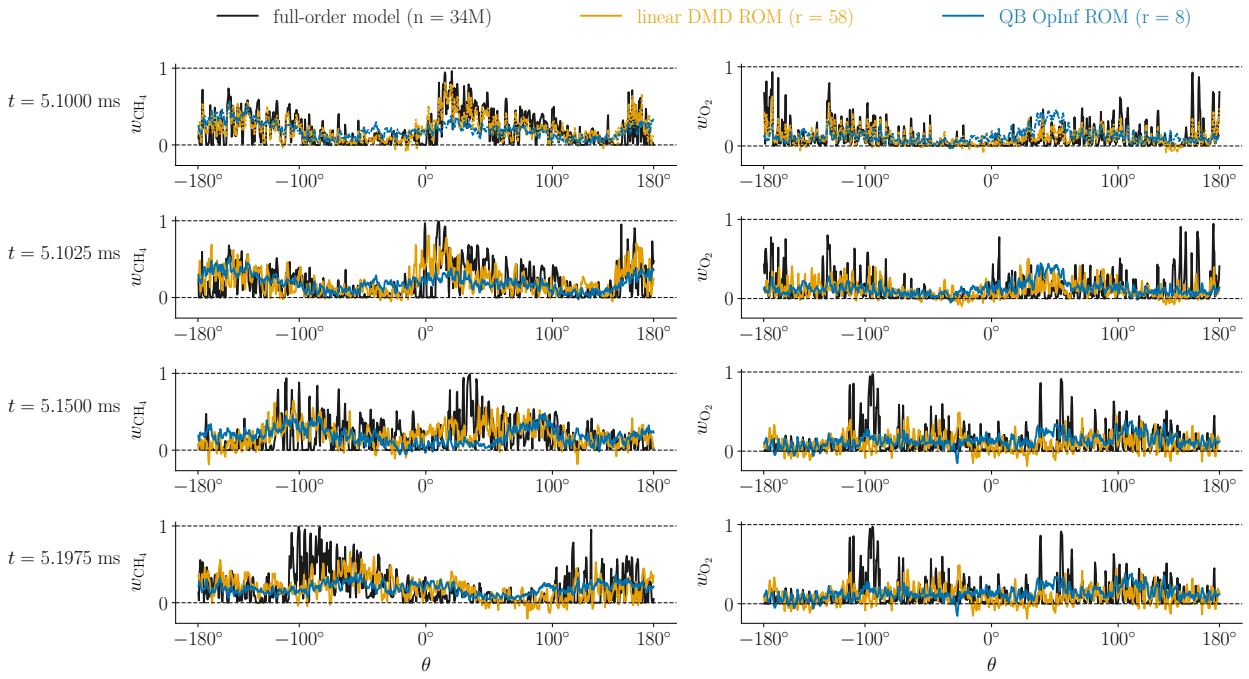

Fig. 17 Second injector design: ROM predictions of one-dimensional circumferential fuel (left column) and oxidizer (right column) mass fraction profiles close to the injectors, at mid-channel, for $\mu_1 = 1.41$. The rows plot the results at four time instants: the last time instant in the training horizon (plotted using dashed lines) and three time instants in the prediction horizon.

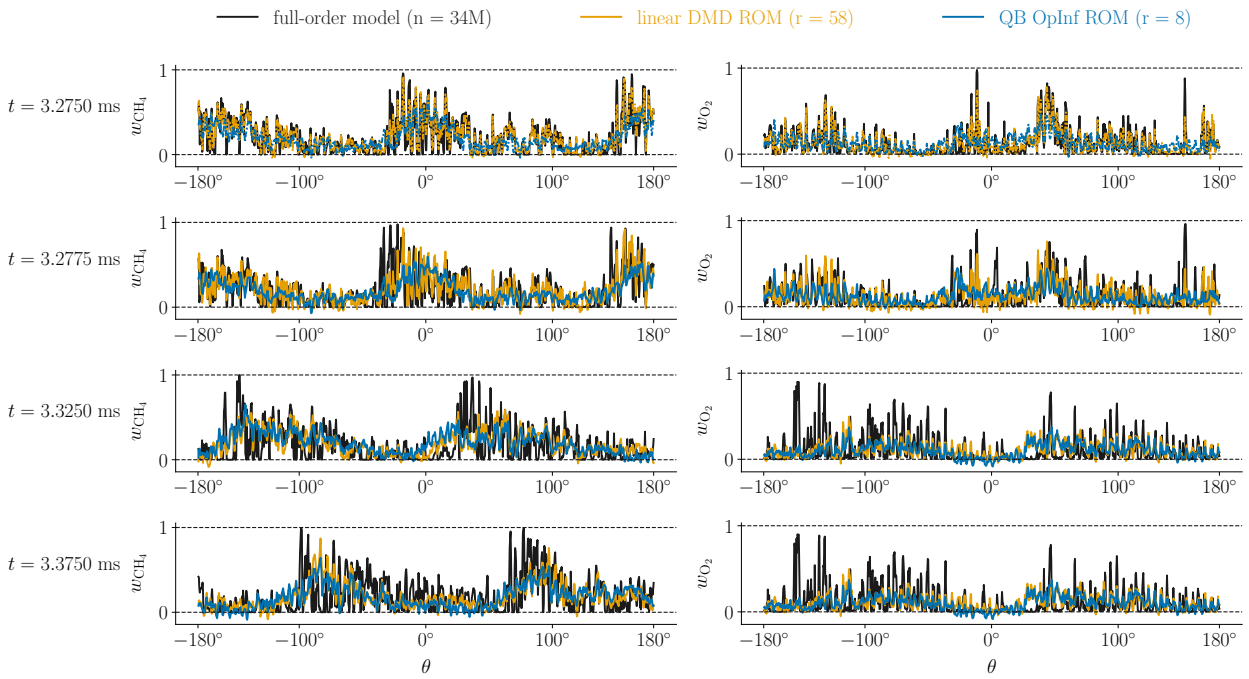

Fig. 18 Second injector design: ROM predictions of one-dimensional circumferential fuel (left column) and oxidizer (right column) mass fraction profiles close to the injectors, at mid-channel, for $\mu_2 = 1.60$. The rows plot the results at four time instants: the last time instant in the training horizon (plotted using dashed lines) and three time instants in the prediction horizon.

Distribution Statement A: Approved for Public Release; Distribution is Unlimited. PA# AFRL-2022-5626

V. Conclusion

This paper took the first steps towards constructing parametric non-intrusive reduced models from data for large-scale rotating detonation rocket engine combustion chambers, with the end goal of using these reduced models to accelerate the design optimization of these devices. To addresses the challenges associated with sparse training data sets containing down-sampled time instants from the high-fidelity simulation codes, available for only a handful of parameter instances, we used a discrete operator inference procedure in which the parametric dependence of the reduced operators were approximated via a Taylor expansion. Our results for two injector designs show that our reduced models are accurate for both parametric predictions and predictions beyond the training horizon. Overall, given the complexity of the scenarios under consideration, our parametric reduced models performed well, which shows that operator inference represents a practically viable approach for constructing from data accurate and predictive parametric reduced models for large-scale, realistic detonation rocket engine combustion chambers. Should reduced models provide means to decrease the cost of a computationally complex system such as the rotating detonation engine by optimally utilizing high fidelity simulation data, this success can have strong implications in a number of allied fields in aerospace propulsion. The requirements we place on the level of accuracy and the resolution of multiscale features in parametric reduced models still remains to be determined, following an actual implementation of these methods in a design setting.

Acknowledgments

This work was supported in part by AFRL Grant FA9300-22-1-0001 and the Air Force Center of Excellence on Multifidelity Modeling of Rocket Combustor Dynamics under grant FA9550-17-1-0195.

References

[1] Bykovskii, F., Zhdan, S., and Vedernikov, E., "Continuous Spin Detonations," *Journal of Propulsion and Power*, Vol. 22, 2006, pp. 1204–1216. https://doi.org/10.2514/1.17656.

[2] Benner, P., Gugercin, S., and Willcox, K., "A Survey of Projection-Based Model Reduction Methods for Parametric Dynamical Systems," *SIAM Review*, Vol. 57, No. 4, 2015, pp. 483–531. https://doi.org/10.1137/130932715.

[3] Bui-Thanh, T., Willcox, K., and Ghattas, O., "Parametric Reduced-Order Models for Probabilistic Analysis of Unsteady Aerodynamic Applications," *AIAA Journal*, Vol. 46, No. 10, 2008, pp. 2520–2529. https://doi.org/10.2514/1.35850.

[4] Chen, Z., Zhao, Y., and Huang, R., "Parametric reduced-order modeling of unsteady aerodynamics for hypersonic vehicles," *Aerospace Science and Technology*, Vol. 87, 2019, pp. 1–14. https://doi.org/https://doi.org/10.1016/j.ast.2019.01.035.

[5] Goizueta, N., Wynn, A., and Palacios, R., "Adaptive Sampling for Interpolation of Reduced-Order Aeroelastic Systems," *AIAA Journal*, Vol. 60, No. 11, 2022, pp. 6183–6202. https://doi.org/10.2514/1.J062050.

[6] Amsallem, D., and Farhat, C., "An Online Method for Interpolating Linear Parametric Reduced-Order Models," *SIAM Journal on Scientific Computing*, Vol. 33, No. 5, 2011, pp. 2169–2198. https://doi.org/10.1137/100813051.

[7] Renganathan, S. A., Maulik, R., and Rao, V., "Machine learning for nonintrusive model order reduction of the parametric inviscid transonic flow past an airfoil," *Physics of Fluids*, Vol. 32, No. 4, 2020, p. 047110. https://doi.org/10.1063/1.5144661.

[8] Rajaram, D., Perron, C., Puranik, T. G., and Mavris, D. N., "Randomized Algorithms for Non-Intrusive Parametric Reduced Order Modeling," *AIAA Journal*, Vol. 58, No. 12, 2020, pp. 5389–5407. https://doi.org/10.2514/1.J059616.

[9] Renganathan, S. A., "Koopman-Based Approach to Nonintrusive Reduced Order Modeling: Application to Aerodynamic Shape Optimization and Uncertainty Propagation," *AIAA Journal*, Vol. 58, No. 5, 2020, pp. 2221–2235. https://doi.org/10.2514/1.J058744.

[10] Maraniello, S., and Palacios, R., "Parametric Reduced-Order Modeling of the Unsteady Vortex-Lattice Method," *AIAA Journal*, Vol. 58, No. 5, 2020, pp. 2206–2220. https://doi.org/10.2514/1.J058894.

[11] Peherstorfer, B., and Willcox, K., "Data-driven operator inference for nonintrusive projection-based model reduction," *Computer Methods in Applied Mechanics and Engineering*, Vol. 306, 2016, pp. 196–215. https://doi.org/https://doi.org/10.1016/j.cma.2016.03.025.

[12] Qian, E., Kramer, B., Peherstorfer, B., and Willcox, K., "Lift & Learn: Physics-informed machine learning for large-scale nonlinear dynamical systems," *Physica D: Nonlinear Phenomena*, Vol. 406, 2020, p. 132401. https://doi.org/https://doi.org/10.1016/j.physd.2020.132401.

Distribution Statement A: Approved for Public Release; Distribution is Unlimited. PA# AFRL-2022-5626

[13] Swischuk, R., Kramer, B., Huang, C., and Willcox, K., "Learning Physics-Based Reduced-Order Models for a Single-Injector Combustion Process," *AIAA Journal*, Vol. 58, No. 6, 2020, pp. 2658–2672. https://doi.org/10.2514/1.J058943.

[14] McQuarrie, S. A., Huang, C., and Willcox, K. E., "Data-driven reduced-order models via regularised Operator Inference for a single-injector combustion process," *Journal of the Royal Society of New Zealand*, Vol. 51, No. 2, 2021, pp. 194–211. https://doi.org/10.1080/03036758.2020.1863237.

[15] Qian, E., Farcaş, I.-G., and Willcox, K., "Reduced Operator Inference for Nonlinear Partial Differential Equations," *SIAM Journal on Scientific Computing*, Vol. 44, No. 4, 2022, pp. A1934–A1959.

[16] Farcas, I., Munipalli, R., and Willcox, K. E., "On filtering in non-intrusive data-driven reduced-order modeling," *AIAA AVIATION 2022 Forum*, AIAA, 2022. https://doi.org/10.2514/6.2022-3487.

[17] Lietz, C., Desai, Y., Munipalli, R., Schumaker, S. A., and Sankaran, V., "Flowfield analysis of a 3D simulation of a rotating detonation rocket engine," *AIAA Scitech 2019 Forum*, 2019. https://doi.org/10.2514/6.2019-1009.

[18] Gu, C., "QLMOR: A Projection-Based Nonlinear Model Order Reduction Approach Using Quadratic-Linear Representation of Nonlinear Systems," *IEEE Transactions on Computer-Aided Design of Integrated Circuits and Systems*, Vol. 30, No. 9, 2011, pp. 1307–1320. https://doi.org/10.1109/TCAD.2011.2142184.

[19] Benner, P., Goyal, P., and Gugercin, S., "$\mathcal{H}_2$-Quasi-Optimal Model Order Reduction for Quadratic-Bilinear Control Systems," *SIAM Journal on Matrix Analysis and Applications*, Vol. 39, No. 2, 2018, pp. 983–1032. https://doi.org/10.1137/16M1098280.

[20] Kramer, B., and Willcox, K. E., "Nonlinear Model Order Reduction via Lifting Transformations and Proper Orthogonal Decomposition," *AIAA Journal*, Vol. 57, No. 6, 2019, pp. 2297–2307. https://doi.org/10.2514/1.J057791.

[21] Tu, J. H., Rowley, C. W., Luchtenburg, D. M., Brunton, S. L., and Kutz, J. N., "On dynamic mode decomposition: Theory and applications," *Journal of Computational Dynamics*, Vol. 1, No. 2, 2014, pp. 391–421.

[22] Kutz, J. N., Brunton, S. L., Brunton, B. W., and Proctor, J. L., *Dynamic Mode Decomposition*, Society for Industrial and Applied Mathematics, Philadelphia, PA, 2016. https://doi.org/10.1137/1.9781611974508.

[23] Batista, A., Ross, M., Lietz, C., and Hargus, W. A., "Detonation Wave Interaction Classification in a Rotating Detonation Rocket Engine," *AIAA Propulsion and Energy 2020 Forum*, 2020. https://doi.org/10.2514/6.2020-3861.

[24] Smith, G. P., Tao, Y., and Wang, H., "Foundational Fuel Chemistry Model Version 1.0 (FFCM-1)," , 2016. URL http://nanoenergy.stanford.edu/ffcm1.

[25] Westbrook, C. K., and Dryer, F. L., "Chemical kinetic modeling of hydrocarbon combustion," *Progress in Energy and Combustion Science*, Vol. 10, 1984, pp. 1–57. https://doi.org/10.1016/0360-1285(84)90118-7.

[26] Bigler, B., Bennewitz, J., Danczyk, S., and Hargus, W., "Rotating Detonation Rocket Engine Operability Under Varied Pressure Drop Injection," *Journal of Spacecraft and Rockets*, Vol. 58, 2021, pp. 1–10. https://doi.org/10.2514/1.A34763.

[27] Mezić, I., "Spectral Properties of Dynamical Systems, Model Reduction and Decompositions," *Nonlinear Dynamics*, Vol. 41, No. 1, 2005, pp. 309–325. https://doi.org/10.1007/s11071-005-2824-x.

[28] Mezić, I., "Analysis of Fluid Flows via Spectral Properties of the Koopman Operator," *Annual Review of Fluid Mechanics*, Vol. 45, No. 1, 2013, pp. 357–378. https://doi.org/10.1146/annurev-fluid-011212-140652.

Distribution Statement A: Approved for Public Release; Distribution is Unlimited. PA# AFRL-2022-5626